PAPER

Understanding the mechanisms of *L*-shell x-ray emission from Os atoms bombarded by 4–6 MeV/u fluorine ion

Physica Scripta

PAPER

Understanding the mechanisms of *L*-shell x-ray emission from Os atoms bombarded by 4–6 MeV/u fluorine ion

RECEIVED
22 December 2021

REVISED
17 February 2022

ACCEPTED FOR PUBLICATION
21 February 2022

PUBLISHED
4 March 2022

Soumya Chatterjee[1], **Sunil Kumar**[2], **Sarvesh Kumar**[3], **M Oswal**[4], **Biraja Mohanty**[5], **D Mehta**[5], **D Mitra**[1], **A M P Mendez**[6], **D M Mitnik**[6], **C C Montanari**[6], **L Sarkadi**[7] and **T Nandi**[8,9]

[1] Department of Physics, University of Kalyani, Kalyani, West Bengal-741235, India
[2] Govt College Kullu, Himachal Pradesh 175101, India
[3] Laboratório de Colisões Atómicas e Moleculares (LACAM), CEFITEC, Department of Physics, Nova School of Science and Technology, Universidade NOVA de Lisboa, 2829-516 Caparica, Portugal
[4] Department of physics, DAV College, Sector 10, Chandigarh 160011, India
[5] Department of Physics, Panjab University, Chandigarh-160014, India
[6] Instituto de Astronomía y Física del Espacio, CONICET and Universidad de Buenos Aires, Buenos Aires, Argentina
[7] Institute for Nuclear Research of the Hungarian Academy of Sciences (MTA Atomki), H-4001 Debrecen, Pf. 51, Hungary
[8] Inter-University Accelerator Centre, Aruna Asaf Ali Marg, Near Vasant Kunj, New Delhi-110067, India
[9] Present address: 1003 Regal, Mapsko Royal Ville, Sector-82, Gurgaon-122004, India.

E-mail: nanditapan@gmail.com

Keywords: electron capture, multiple ionization, charge state distribution

Abstract

The *L*-subshell ionization mechanism is studied in an ultra-thin Os target bombarded by 4–6 MeV/u fluorine ions. Multiple ionization effects are considered through the change of fluorescence and Coster-Kronig yields while determining *L*-subshell ionization cross sections from *L* x-ray production cross sections. The present experimental values are compared with various theoretical approximations: (i) the relativistic semi-classical approximation (RSCA), (ii) the shellwise local plasma approximation (SLPA), and (iii) the ECUSAR theory. We also take into account the vacancy sharing among the subshells by the coupled-states model (CSM) and the electron capture (EC) by a standard formalism. We find that the ECUSAR-CSM-EC describes the measured excitation function curves the best. However, the theoretical calculations are still about a factor of two smaller than the measured values even though the recent fluorescence and Coster-Kronig yields are considered. Hence, a re-evaluation of these parameters is a challenge for the theoretical works. Whatsoever, this work leads to demonstrate that in the present energy range the heavy-ion induced inner-shell ionization of the heavy atoms can be understood by combining the direct Coulomb ionization, the electron capture, and the vacancy sharing among subshells, together with optimizing the atomic parameters. Optimization of the atomic parameters shows that our experimental results agree with theoretical vacancy production theories if the L1 fluorescence yield is nearly doubled. Such a optimization is validated by the proton induced L-shell ionization data of uranium atoms.

1. Introduction

The measurement of emitted x-rays from targets has resulted in major advances in radiation physics [1], plasma physics [2], atomic and nuclear physics [3], and the particle-induced x-ray emission (PIXE) technique [4, 5]. Thus far, the PIXE method has used light ions such as protons or alphas [6–13]; however, there is an increasing interest to employ heavy ions since their cross sections are larger and have, thereby, better sensitivity [14]. Nevertheless, this potentiality is discouraged by discrepancies observed between the theories and experiments. Although these inconsistencies are often attributed to multiple ionization phenomena [15–17], they do not account for all the discrepancies observed, for example, in experiments with an 8–36 MeV Si-ion beam on targets of Au, Bi, Th, and U with thicknesses between 12 and 40 μ g/cm^2 [18]. On such occasions, theoretical approaches have been modified to include the *L*-subshell coupling effect as well as the saturation of the binding

effect at the united atom limit in addition to the multiple ionization [18, 19]. Even though closeness between the experiments and theory is achieved, differences remain, suggesting that other physical processes are involved.

It is well-known that for asymmetric collisions, $Z_1/Z_2 < 1$, the direct ionization (DI) is dominant, whereas for symmetric collisions, $Z_1/Z_2 \approx 1$, the electron capture (EC) process becomes increasingly important. Although the present collisional system is asymmetric, i.e. F ions ($Z_1 = 9$) impinging on Os ($Z_2 = 76$), and $Z_1/Z_2 = 0.1184$, the EC contribution to the L-shell vacancy production has to be accounted [20]. This becomes evident if we consider the ratio of the projectile velocity v_1 to the orbital velocity of the target electrons, v_{L_i}. In our full-relativistic calculations [21], the mean velocities (in a.u.) of the Os L_i sub-shells are $v_{L_i} = 26.6, 37.7$, and 32.8 for $i = 1, 2, 3$, respectively. Therefore, $0.33 \leqslant v_1/v_{L_i} \leqslant 0.58$, and the collision is asymmetric but in the slow velocity regime.

We studied L-subshell vacancy production by considering the DI, the multiple ionization, and the vacancy sharing by performing a detailed experimental-theoretical comparison. We found a general tendency of the models to underestimate the data. However, contrary to our expectations, the EC does not account for all the discrepancies found. In the final stage of this work, we found that the presently available atomic parameters (the fluorescence and Coster-Kronig yields) are unable to achieve agreement between the experiment and the theory. So, we modified these values iteratively until a good agreement between them was achieved.

We provide experimental details in section 2. The theoretical methods employed to describe the direct ionization are discussed in section 3. Section 4 addresses the effects of the single- and multiple-hole atomic parameters required for the derivation of the subshell-ionization cross sections from the measured x-ray production cross sections. Section 5 describes the main capture processes involved, and how they were theoretically evaluated. Finally, section 6 summarizes the major findings.

2. Experimental details and data analysis

The L-shell x-ray production cross sections in the Os elements using the ^{19}F ions (charge states $q = 6+, 7+, 8+$) in the 76–114 MeV energy range have been measured in the atomic physics beamline at the Inter-University Accelerator Centre, New Delhi. The heavy ions of fluorine –F^{6+} (76 and 84 MeV), F^{7+} (90 MeV) and F^{8+} (98 and 114 MeV)–were obtained from the 15 UD Pelletron accelerator. The chamber has provision for two silicon surface barrier (SSB) detectors at $\pm$ 7.5° and two x-ray detectors at 55° and 125° to the beam direction, respectively. The target was mounted on a steel ladder forming a 90° angle to the beam direction. The vacuum inside the chamber was $\sim 10^{-6}$ Torr. The spot of the ion beam at the target had a diameter of approximately 2 mm. The spectra were taken at different positions of each target. Details of the experimental setup and detection system are given by Kumar *et al* [22]. The ultra-thin target of $_{76}$Os was prepared on the polypropylene backing using an ultra-high vacuum deposition setup at IUAC, New Delhi. The thickness of the target was measured using the Rutherford Back-scattering (RBS) method and its spectrum is given in figure 1. The target turned out to be very thin, only 1.09 μg/cm^2. The beam current was kept below 1 nA to avoid pile up effects and damage to the target. The spectra were collected for a long time to get barely sufficient statistics and thus obtained a decent accuracy for the production cross sections. We obtained L x-ray spectra of natural Os bombarded by F^{q+} at different projectile energies (76–114 MeV). Among them spectrum for 90 MeV is shown in figure 2. The spectra were analyzed with a fitting method considering a Gaussian line shape for the x-ray peaks and a suitable background function. From the figures, it is clear that all major L x-ray components are well resolved by the Si(Li) detector. The details about the data acquisitions and the terms related to the projectile velocity are given by Oswal *et al* [23].

The measured L x-ray production cross sections for the major peaks namely L_l, L_η, L_α, L_β, and $L\gamma$ were obtained using the following relation

$$\sigma_x^i = \frac{Y_x^i\, A}{N_A\, n_p\, t\, \epsilon\, \beta} \sin\theta, \tag{1}$$

where Y_x^i is the intensity of the ith x-ray peak, A is the atomic weight of the target, θ is the angle between the incident ion beam and the target foil surface, N_A is the Avogadro number, n_p is the number of incident projectiles, ϵ is the effective efficiency of the x-ray detector, t is the target thickness 1.09 μg/cm^2 and β is a correction factor for the absorption of the emitted x-rays inside the target.

The absorption correction factor for the absorption of the emitted L x-rays in the target is written as

$$\beta = \frac{1 - \exp(-\mu t)}{\mu t}, \tag{2}$$

where μ is the attenuation coefficient inside the target and its unit is cm^2/g [24]. The value of β is $\geqslant 0.99$ for the target thickness used in the present measurements. The energy loss calculation using the SRIM code [25] for the

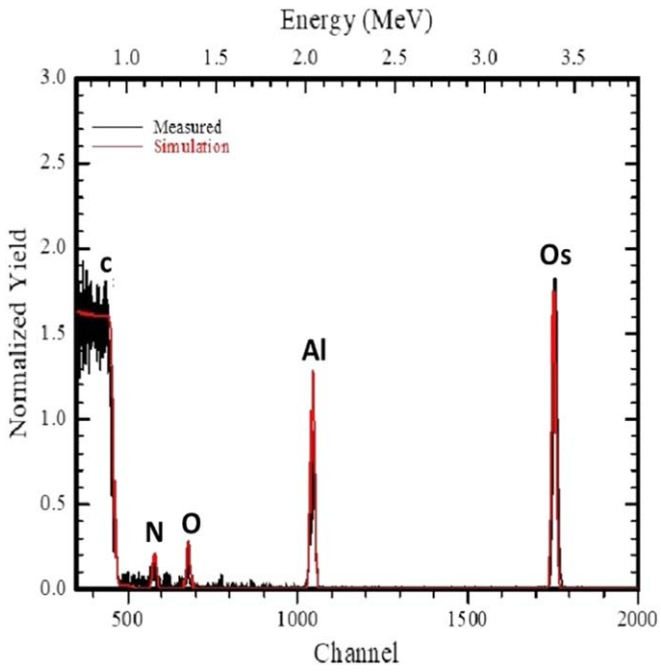

Figure 1. The Rutherford backscattering spectrum of the Os target by ^{4}He ion impact.

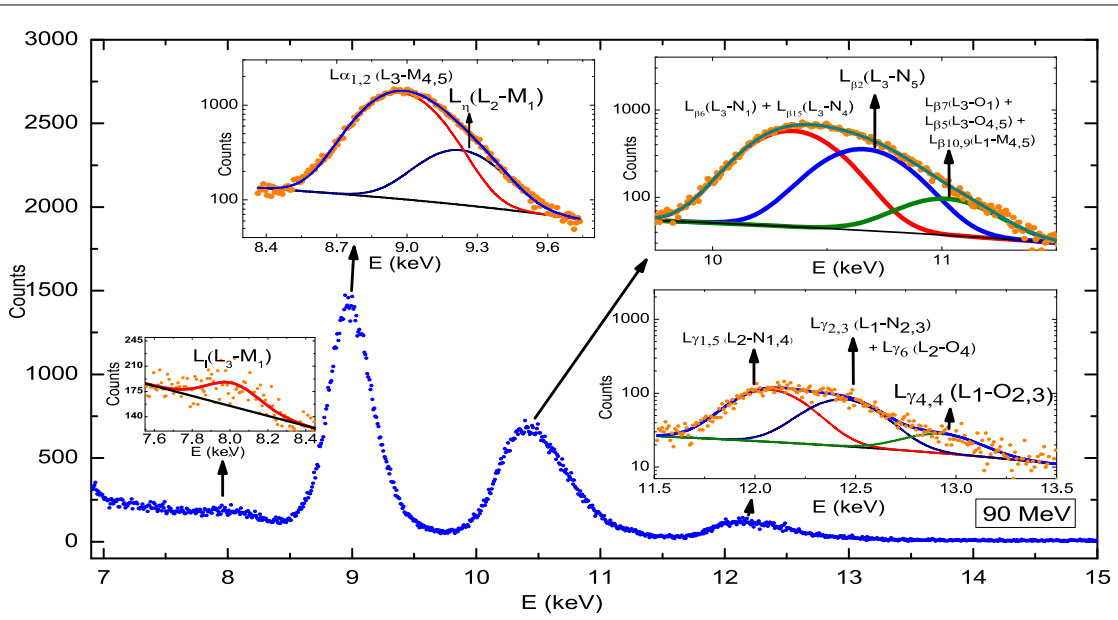

Figure 2. The *L* x-ray spectra of the Os target bombarded by ^{19}F ions of energy 90 MeV. *Ll*, *Lα*, *Lβ* and *Lγ* spectrum fittings are shown in insets.

incident beam within the target suggests negligibly small energy loss for the target thickness and the beam energies used in the present work. The ion beam changes its charge state during its passage through the target.

The role of projectile charge state in this collision regime for 4–6 MeV/u is found to be negligible [23]. Integrated charge in a Faraday cup measured by a current integrator has been used to count N_p (see discussion in section 6). The energy loss calculation using the SRIM code shows that 76 and 114 MeV fluorine ions lose 2.30 and 1.91 keV in the Os target, respectively. The peak areas Y_x^i are evaluated using the computer program CANDLE [26]. This software is an improved version of the Levenburg-Marquardt [27] non-linear minimization algorithms for the peak fitting. The energy calibration of the detector is performed before and after the in-beam measurements. A semi-empirical fitted relative efficiency curve for the present measurement is available in Oswal *et al* [23].

The percentage error in the measured x-ray production cross sections is about 15%–20%. This error is attributed to the uncertainties in different parameters used in the analysis, namely the photo peak area evaluation (~3% for the L_α, ~4% for the L_β, ~11% for the L_γ x-ray peak and 7% for the Ll), ion beam current (~7%), and target thickness (~3%). In the energy region of interest, the error of the absolute efficiency values ϵ ranges between 5% and 8%.

3. Ionization theories

To calculate the DI cross sections, we have employed (i) the coupled-states relativistic semi-classical approximation (RSCA-CSM) [28, 29], (ii) the ECPSSR and the ECUSAR theory [30, 31] and iii) the shellwise local plasma approximation (SLPA) [32, 33] with fully relativistic electronic structure calculations for Os [21]. It is worth noting that RSCA-CSM and SLPA are *ab initio* methods, while ECUSAR is semiempirical. All these models are briefly described below.

3.1. The coupled-states relativistic SCA model (RSCA-CSM)

In the semi-classical approximation (SCA), the general form of the cross section is expressed as follows

$$\sigma_i = 2\pi \int_0^\infty \mathrm{d}b\; b \sum_f |a_f(t=+\infty)|^2, \tag{3}$$

where b is the impact parameter, and $a_f(t)$ is the excitation amplitude of the L_i sub-state to a final f state. For the continuum states, the sum means integration over the electron energy. Applying the *independent-particle model* approximation, the many-electron excitation amplitudes are replaced by single-electron transition amplitudes.

The subshell coupling mechanism is described in a way that a 'mixed' L state is considered as the initial state, instead of a 'pure' atomic state [28]. The mixed state evolves in time from the initial L-substate as a result of dynamical couplings with the other L-substates. The time evolution is governed by the following eight coupled equations (in a.u.):

$$\frac{\mathrm{d}a_{n_L}}{\mathrm{d}t} = -i \sum_{n_L'} \mathcal{V}_{n_L n_L'} a_{n_L'}, \tag{4}$$

with the initial condition

$$a_{n_L}(t=-\infty) = \delta_{n_L i}. \tag{5}$$

The excitation from the mixed L-substate to the f final state is described by

$$\frac{\mathrm{d}a_f}{\mathrm{d}t} = -i \sum_{n_L} \mathcal{V}_{f n_L} a_{n_L}. \tag{6}$$

In equations (4) to (6), n_L represents the quantum numbers (l, j, m_j) of the L substates. The $\mathcal{V}_{mk}(t)$ matrix elements for the projectile-target-electron interaction are defined as

$$\mathcal{V}_{mk}(t) = V_{mk}(t) \exp(i\omega_{mk} t), \tag{7}$$

$$V_{mk}(t) = \int \mathrm{d}\mathbf{r}\; \psi_m^*(\mathbf{r}) \frac{-Z_1}{|\mathbf{r} - \mathbf{R}(t, b)|} \psi_k(\mathbf{r}), \tag{8}$$

$$\omega_{mk} = E_m - E_k, \tag{9}$$

where Z_1 is the atomic number of the projectile, $\mathbf{R}$ is the internuclear vector, and $\psi_j(\mathbf{r})$ and E_j are the one-electron energy eigenstates and eigenvalues of the unperturbed target atom. For $\mathbf{R}(\mathbf{t}, \mathbf{b})$, a Kepler projectile orbit is applied.

In the present SCA model, the V_{mk} matrix elements are calculated using screened relativistic wave functions for both the bound and continuum states [29], i.e., it is an RSCA model. Furthermore, since it includes the subshell coupling effects, the full name of the model is coupled-states RSCA, briefly: RSCA-CSM.

We stress that unlike previous works (see, e.g., [34, 35]), the integration over the final states in equation (3) is complete, and the present RSCA-CSM calculation extends to the entire range of the energy transfer. Additionally, no restrictions are imposed on the angular momentum of the ionized electron.

3.2. ECPSSR/ECUSAR-CSM model

The ECPSSR model by Brandt and Lapicki [30] and its evolution into the ECUSAR model [31] are the most employed theories to describe inner-shell ionization cross sections. They cover an extended energy range, and are the usual input values in PIXE codes [31]. The ECPSSR theory goes beyond the plane-wave Born approximation (PWBA) by accounting for the energy loss (E), the Coulomb deflection from a straight-line

trajectory and retardation of the projectile (C) and its influence on the unperturbed and non-relativistic atomic orbitals in a perturbed stationary state (PSS) treatment that also accounts for the relativistic (R) nature of the inner shells of heavy target atom. In the ECUSAR theory of Lapicki [31], the PSS treatment of ECPSSR [30] is replaced by the united (U) and separated (S) atom (A) formula (see equations (2) and (3) in [31]).

Comparing RSCA-CSM [34] to ECPSSR [30], one has to stress that the former automatically incorporates most of the effects that are included in ECPSSR as corrections. The application of Kepler orbit accounts for the Coulomb-deflection effect. The diagonal matrix elements V_{mk} determine in a first-order approximation the change of the binding energies of the L substates in the presence of the projectile, i.e., they account for the increased binding effect, which is one of the most important consequences of the PSS approach. And, of course, the electronic relativistic effects are exactly taken into account. At the same time, there are differences between the two theories (in addition to the subshell couplings). The ECPSSR model [30] is based on the plane-wave Born approximation (PWBA). Although the PWBA and the straight-line SCA are equivalent, this feature holds only for the hydrogen atom, or hydrogenic ions. For a many-electron atom, it is known that the screening procedure is different for the two theories. It can be shown that the outer screening applied in PWBA leads to an effective potential that approaches the many-electron potential better than the corresponding effective potential in SCA. Furthermore, the energy loss effect is not included in the RSCA-CSM, i.e., one does not expect a good performance of the model at very low collision velocities.

In light of the above arguments, the best description of the ion-induced L-shell ionization is expected to be given by a modified ECPSSR that includes the subshell coupling effects. Such a model, named ECPSSR-CSM, is obtained by combining ECPSSR and RSCA-CSM in the following way. The original idea behind considering the couplings between the L substates was the vacancy sharing process among the L subshells. The vacancy sharing does not change the total L-shell ionization cross section, which is supposed to be described well by ECPSSR. At the same time, the relative subshell ionization cross sections change according to RSCA-CSM. This concept can be expressed by renormalizing the RSCA-CSM subshell cross sections in a way that its sum equals the total ECPSSR cross section (see also [36]),

$$\sigma_{Li}(\mathrm{ECPSSR-CSM}) = \sigma_{Li}(\mathrm{RSCA-CSM}) \times \frac{\sigma_{\mathrm{Tot}}(\mathrm{ECPSSR-CSM})}{\sigma_{\mathrm{Tot}}(\mathrm{RSCA-CSM})}. \tag{10}$$

In the present work, we applied the improved version of ECPSSR, the ECUSAR model. According to equation (10), the subshell coupling effects are also included in the latter model.

3.3. Shellwise local plasma approximation (SLPA)

The shellwise local plasma approximation (SLPA) [32, 33] is an ab-initio approach for the calculation of ionization probabilities within the dielectric formalism. It is a collective model based on the quantum dielectric response theory, which accounts for the inner-shells by considering the density of target electrons and the binding energies. The SLPA calculates the j subshell ionization cross section of target atoms due to the interaction with a projectile (velocity v_1 and nuclear charge Z_1) as

$$\sigma_j^{\mathrm{SLPA}} = 2/(\pi v_1^2)\int_0^\infty \frac{Z_1^2}{p}dp \int_0^{pv_1} d\omega \times \int Im\left[\frac{-1}{\epsilon\,(p,\,\omega,\,E_j,\,\delta_j(r)}\right]\vec{dr}, \tag{11}$$

with $\epsilon(p, \omega, E_j, \delta_j)$ being the Levine-Louie dielectric function [37], E_j the binding energy, $\delta_j(r)$ the density of the j-subshell electrons around the nucleus, and $p(w)$ the momentum (energy) transferred.

The electronic densities and binding energies of the L_i subshells of Os were obtained by performing full relativistic atomic structure calculations. We solved the Dirac equation by implementing the parametric potential method [38–40] and an optimized configuration interaction mixing. The electronic structure so computed agrees with available experimental values within 1.5% [21]. It is worth noting that the SLPA has been successfully employed previously by the authors to obtain L-shell ionization cross sections of relativistic targets such as Pt, Ta, W, Pb, Au, Bi, Th and U [23, 41].

3.4. Method for obtaining theoretical x-ray production cross section from theoretical L-shell ionization cross section

The theoretical L x-ray production cross sections for the most commonly resolved L_l, L_α, L_β, L_γ x-rays are related to the L_i subshell ionization cross sections, σ_{Li}, as given below

$$\sigma_{L_l}^x = [\sigma_{L_1}(f_{13} + (f_{12}f_{23}) + \sigma_{L_2}f_{23} + \sigma_{L_3}]\omega_3 F_{3l}, \tag{12}$$

Table 1. The fluorescence and CK yields for the singly-ionized Os are denoted by superscript 0 (ω_i^0, f_{ij}^0) and when these are optimized they are denoted by superscript $0m$ (ω_i^{0m}, f_{ij}^{0m}). The values listed for the singly-ionized atoms were taken from the compilation of Campbell [43]. When the fluorescence and CK yield values corrected on account of the SMI the superscript 0 is dropped and thus, $\omega_i^0 \rightarrow \omega_i$, $f_{ij}^0 \rightarrow f_{ij}$ and $\omega_i^{0m} \rightarrow \omega_i^m$, $f_{ij}^{0m} \rightarrow f_{ij}^m$. Note that the optimized parameters resulted in the best agreement between the theoretical and experimental L-subshell ionization cross sections (see text).

Atomic Number (Z)		Fluorescence Yield						CK Yield					
						SI							
76		ω_1^0	ω_1^{0m}	ω_2^0	ω_2^{0m}	ω_3^0	ω_3^{0m}	f_{12}^0	f_{12}^{0m}	f_{13}^0	f_{13}^{0m}	f_{23}^0	f_{23}^{0m}
		0.15	0.279	0.318	0.34	0.282	0.305	0.07	0.08	0.33	0.36	0.13	0.17
						MI							
E (MeV)	Q_m	ω_1	ω_1^m	ω_2	ω_2^m	ω_3	ω_3^m	f_{12}	f_{12}^m	f_{13}	f_{13}^m	f_{23}	f_{23}^m
76	8.73	0.196	0.348	0.392	0.416	0.352	0.377	0.0367	0.0441	0.173	0.19	0.0682	0.0892
84	8.74	0.190	0.34	0.383	0.407	0.344	0.369	0.0394	0.0473	0.186	0.204	0.0732	0.0957
90	8.75	0.187	0.336	0.378	0.402	0.339	0.364	0.0411	0.0493	0.194	0.213	0.0763	0.0998
98	8.76	0.184	0.33	0.373	0.396	0.333	0.359	0.0431	0.0518	0.203	0.224	0.0801	0.105
114	8.78	0.178	0.322	0.364	0.388	0.325	0.350	0.0464	0.0570	0.219	0.241	0.0862	0.113

$$\sigma_{L_\alpha}^x = [\sigma_{L_1}(f_{13} + (f_{12}f_{23}) + \sigma_{L_2}f_{23} + \sigma_{L_3}]\omega_3 F_{3\alpha}, \tag{13}$$

$$\sigma_{L_\beta}^x = \sigma_{L_1}[\omega_1 F_{1\beta} + f_{12}\omega_2 F_{2\beta} + (f_{13} + (f_{12}f_{23})\omega_3 F_{3\beta}] + \sigma_{L_2}(\omega_2 F_{2\beta} + f_{23}\omega_3 F_{3\beta}) + \sigma_{L_3}\omega_3 F_{3\beta}, \tag{14}$$

and

$$\sigma_{L_\gamma}^x = \sigma_{L_1}\omega_1 F_{1\gamma} + (\sigma_{L_1}f_{12} + \sigma_{L_2})\omega_2 F_{2\gamma}. \tag{15}$$

Here $\sigma_{L_p}^x$ is the x-ray production cross sections of the different L x-ray components, σ_{L_i} is the ionization cross sections for the L_i subshell, ω_i is the fluorescence yields of the L_i subshells, $f_{ij}(i<j)$ is the CK yields for the CK transition between the L_i and L_j subshells, and F_{ip} is the fractional radiative emission rates, with $i = 1, 2, 3$ and $p = l, \alpha, \beta, \gamma$. The theoretical L x-ray production cross sections were calculated by combining the L_i ionization cross sections obtained by the different L-shell ionization models in equations (12) to (15). L_η line corresponds to the L2-M1 transition. Since the branching ratio of this line is only 0.036 which is even much less than L_{γ_1} (L2-N1) line 0.26. So the intensity corresponds to l_η line is negligibly small and not visible in the recorded spectra.

3.5. Method for obtaining experimental L-subshell ionization cross sections from the measured x-ray production cross sections

The L x-ray production cross sections for the most commonly resolved L_ℓ, $L\alpha$, $L\beta$, and $L\gamma$ x rays are related to the $L_i(i = 1, 2, 3)$ subshell ionization cross sections as given below [22]

$$\sigma_{L_1} = \frac{\sigma_{L\gamma 2+3}^x}{\omega_1 S_{\gamma 2+3,1}}, \tag{16}$$

$$\sigma_{L_2} = \frac{\sigma_{L\gamma 1+5}^x}{\omega_2 S_{\gamma 1+5,2}} - \sigma_{L_1}f_{12}, \tag{17}$$

and

$$\sigma_{L_3} = \frac{\sigma_{L\alpha}^x}{\omega_3 S_{\alpha 12,3}} - \sigma_{L_1}(f_{12}f_{23} + f_{13}) - \sigma_{L_2}f_{23}. \tag{18}$$

Here σ_{Lp}^x $(p = \alpha, \gamma_{2+3}, \gamma_{1+5})$ are the x-ray production cross sections of the different L x-ray components, $\sigma_{Li}(i = 1-3)$ are the ionization cross sections for the L_i subshells ($2s_{1/2}$, $2p_{1/2}$, $2p_{3/2}$ respectively), $\omega_i(i = 1-3)$ are the fluorescence yields, $f_{ij}(i<j)$ are the yields for the CK transition between the L_i and L_j subshells, and $S_{pi}(i = 1-3, p = \alpha, \gamma_{2+3}, \gamma_{1+5})$ are the fractional radiative emission rates.

We have used the most recent values of the L x-ray emission rates from Campbell and Wang (1989) [42] for the present work. The single-hole fluorescence ω_i^0 and CK yields f_{ij}^0 have been taken from [43, 44] singly-ionized atom, as displayed in table 1. Now both $L_1(2s_{1/2})$ and $L_2(2p_{1/2})$ subshells are responsible for L_γ complex transitions. According to equations (16) to (18), the production cross sections of the resolved constituents of L_γ line, along with the production cross sections of $L\alpha$ peak containing the transition due to L_3 subshell can be used to obtain the ionization cross sections for all the three subshells. From equation (16), it is obvious that $L\gamma_{2+3}$ production cross section is needed in order to get L_1 sub-shell ionization cross section. But due to the limited energy resolution of the x-ray detectors, the $L\gamma$ peak is resolved into 3 components (i.e. $L\gamma_{1+5}$, $L\gamma_{2,3,6}$ and $L\gamma_{4,4'}$).

So, the contribution coming from the $L\gamma_6$ peak must be subtracted from the experimentally obtained $L\gamma_{2,3,6}$ line, in order to get the yield of the $L\gamma_{2,3}$ line. From the ratio of the radiative transition probabilities (i.e. $\Gamma\gamma_6/\Gamma\gamma_{1,5}$) [42] and the yield of the $L\gamma_{1,5}$ line, the contribution of $L\gamma_6$ line has been obtained and then subtracted from the $L\gamma_{2,3,6}$ line yield.

4. Effect of the multiple vacancies on the atomic parameters used for the conversion of the ionization cross sections to x-ray production cross sections.

Heavy ion induced target ionization phenomena create multiple ionization in the outer subshells along with single ionization in the inner shells. Such simultaneous multiple ionization (SMI) in the target atom changes the atomic parameters: the fluorescence yields and the CK yields, which in turn alter the x-ray production cross sections. In the present work, single vacancy fluorescence yields ω_i^0 and CK yields f_{ij}^0 [43], were corrected for the SMI using a model prescribed by Lapicki *et al* [45]. This method is not quite precise. A better approach could be attained by measuring the peak shifts and evaluating the corrected parameters, following a procedure used by Pajek *et al* [46]. However, proton beams were not available in our laboratory to carry out the peak shift measurements. Thus, we could only implement Lapicki's method. Each electron in a manifold of the outer subshells is ionized with a probability P, which is calculated using equation (A3) from [45] as follows

$$P = \frac{q_m^2}{2\beta v_p^2}\left(1 - \frac{\beta}{4v_p^2}\right), \tag{19}$$

where q_m is the equilibrium charge state of the projectile inside the target obtained from Fermi gas model [20], $\beta = 0.9$ and v_p is the velocity of the projectile. Here, the ω_i^0 values due to single vacancy being corrected to ω_i due to the SMI are given by

$$\omega_i = \omega_i^0[1 - P(1 - \omega_i^0)]^{-1}, \tag{20}$$

while the f_{ij} values for multiple ionization are given by

$$f_{ij} = f_{ij}^0[1 - P]^2. \tag{21}$$

Note that the fractional rates F_{ip} remain unchanged because both the partial and the total non-radiative widths are altered by identical factors. According to equations (20) and (21), the single vacancy fluorescence and CK yields depend on the energy and charge state of the projectile ion. The fluorescence and the CK yields for singly- and multiply-ionized Os is given in table 1. It is clear from this table that for the lower and higher energy values, the L_i subshell fluorescence yields are enhanced by ~30%, and the CK yields are reduced up to ~50% from the single vacancy to the multiple-hole atom in Os. Note that the use of different sets of atomic parameters can change the x-ray production cross section by ~30% or more.

5. *L*-Shell ionization cross section due to electron capture

It is well known that DI is not the only mechanism of inner shell vacancy production. In the low energy range of the present measurements, capture process may be also an important contribution to the target electron loss.

In order to estimate the electron capture cross sections from Os L-shell to K-shell of F^q (LK capture), we need to know the charge state q of the projectile inside the solid Os. Here, we report a theoretical methodology to predict the charge state distribution of projectile ions inside a solid target. This approach utilizes a simple Fermi gas model and a parameterization of the Lorentzian charge state distribution widths. To estimate the LK capture cross sections, we used the approach proposed by Lapicki and Losonsky [47] to calculate the KK electron capture cross section. This method is based on the Oppenheimer-Brinkman-Kramers (OBK) approximation [48] with binding and Coulomb deflection corrections at low velocities. However, the LK capture phenomena is more complex than the KK capture since it involves three L-subshells. In a first approximation, we determined the total electron capture by using the average binding energy. Then, the three subshells were resolved by computing a weighted average, as follows:

$$\sigma_{L1}^C = (B_{L1}/\bar{B}) \times \sigma_L^C \times \frac{n_{L1}}{n}, \tag{22}$$

$$\sigma_{L2}^C = (B_{L2}/\bar{B}) \times \sigma_L^C \times \frac{n_{L2}}{n}, \tag{23}$$

$$\sigma_{L3}^C = (B_{L3}/\bar{B}) \times \sigma_L^C \times \frac{n_{L3}}{n}, \tag{24}$$

where σ_{Li}^{C} and B_{Li} denote the shell wise electron capture cross section and the binding energy, respectively. $\bar{B}$ is the average binding energy of the L shell, whereas σ_{L}^{C}, n_{Li} and n represent the total capture cross section for the L shell, the number of electrons in the L_i subshell and the total number of electrons in the L shell, respectively.

Neglecting the change in the binding energy of the K shell electron of the projectile with one versus two K shell vacancies, a statistical scaling is used to calculate the electron transfer cross section for the case of one projectile K-shell vacancy, $\sigma_{L\to K}$, resulting in $\sigma_{L\to 2K}/2$, where $\sigma_{L\to 2K}$ is the production cross section for two projectile K-shell vacancies. In the present experimental condition, v_1 ranges between 12.39 and 15.17, while $v_{2L} = Z_{2L}/n_2 = 35.925$ (in a.u.), n_2 and n_1 are the principal quantum numbers of L and K shell electrons of the target and the projectile atom, respectively. Following Lapicki and Losonsky [47], $\sigma_{L\to 2K}$ can be obtained as

$$\sigma_{L\to 2k} = \frac{1}{3}\sigma^{\mathrm{OBK}}_{L\to 2k}(\theta_L),\ \theta_k = \frac{E_L}{v_{2L}^2 \times 13.6}, \tag{25}$$

with $Z_{2L} = Z_2 - 4.15$ and

$$\sigma^{\mathrm{OBK}}_{L\to 2k}(\theta_k) = \frac{2^9}{5v_1^2}\pi a_0^2 n_1^2 \frac{(v_{1k}v_{2L})^5 Z_1 10^{24}}{[v_{1k}^2 + (v_1^2 + v_{2L}^2 - v_{1k}^2)^2/4v_1^2]^5}, \tag{26}$$

where E_L is the binding energy of L-shell electron of the target (in eV), and the parameters a_0, v_{1k}, Z_1, and Z_2 are the Bohr radius, the K-shell orbital velocity of the projectile ion, atomic number of the projectile and the target atom, respectively.

Due to the charge state distribution inside the target, the effective capture contribution will be $F(q) \times \sigma^{\mathrm{OBK}}_{L\to 2k}(\theta_L)$, for $q = 8+$ and $9+$. Here, $F(q)$ is the charge state fraction of the specific charge state q responsible for the electron capture. However, determining $F(q)$ is a non trivial task. The charge state of the projectile ion inside the target is determined by the interplay between electron capture and loss. Moreover, the charge state distribution so formed is altered when exiting the target. This alteration is mainly governed by the capture that takes place at the exit surface. Hence, there is large difference between the mean charge states (q_m) as well as the charge state distributions, inside and outside the target. Since, the charge state distribution is described by the $F(q)$ as a function of q, $F(q)$ should be given by the fraction of the charge state q inside the solid target in the present context.

To obtain $F(q)$ inside the target, we employed a two-fold procedure. First, we used a Fermi-gas-model based empirical formula to determine the mean charge state, q_m, inside the target [49]

$$q_m = Z_1\left(1 - \frac{v_F}{v_1}\right), \tag{27}$$

where Z_1 and v_F are the projectile atomic number and the Fermi velocity of target electrons, respectively. The value of Fermi velocity (v_F) for Os is 0.68 a.u..

Note that the charge state distribution outside the target is described by the Schiwietz model [50]. To illustrate the difference between the ionization of the projectile ion inside and outside the target, we displayed the q_m predicted by the Fermi-gas-model [49] and by the Schiwietz model [50] in figure 3(A). This contrasting picture is governed by the solid surface [51, 52], as mentioned above. The charge state of the heavy projectiles is higher inside than outside the target. This feature has been described in detail by Chatterjee *et al* [20] in the context of K x-ray emission.

In the second part of the procedure, the q_m values inside the target are substituted by a Lorentzian charge state distribution [51] to obtain the $F(q)$ as follows

$$F(q) = \frac{1}{2\pi}\frac{\Gamma}{(q - q_m)^2 + (\Gamma/2)^2} \quad \text{and} \quad \sum_q F(q) = 1. \tag{28}$$

The distribution width Γ is taken from Novikov and Teplova [53] as follows

$$\Gamma(x) = C[1 - \exp(-x^{\alpha})]\{1 - \exp[-(1 - x)^{\beta}]\}, \tag{29}$$

where $x = q_m/Z_1$, $\alpha = 0.23$, $\beta = 0.32$ and $C = 2.669 - 0.0098\,Z_2 + 0.058\,Z_1 + 0.00048\,Z_1\,Z_2$. The $F(q)$ for $q = 8+$ and $9+$ are displayed with a bar chart in figure 3(B). Similarly, if we substitute q_m outside the target, we obtain the charge state distributions outside the target.

6. Results and discussions

Present L-shell ionization cross sections are displayed in figure 5(A), and table 2. The data include the present measurements and the three theoretical results, with and without the electron capture contribution. In general, the models underestimate the data, but the ECUSAR results are the most accurate ones. Despite the LK electron capture (EC) effects are included to the various theories, the cross sections remain lower than the measured data.

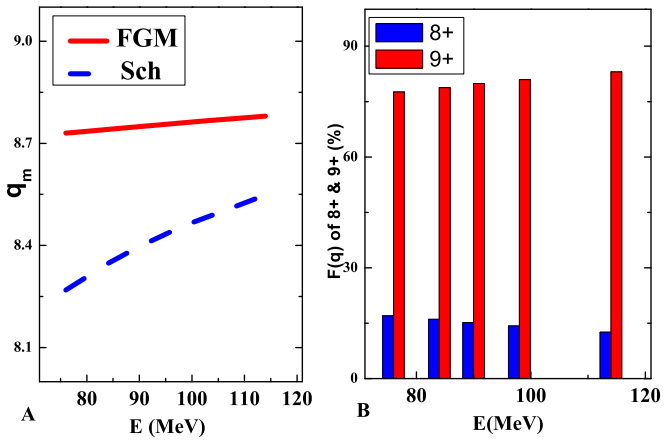

Figure 3. A. The mean charge state of the ^{19}F ion inside the Os target as predicted by the Fermi Gas Model (FGM) [49] and the same outside the target as predicted by the Schiwietz model (Sch) [50] versus the incident energies. B. The charge-state fraction $F(q)$ chart for $q = 8+$ and $9+$ inside the target as a function of the beam energy.

Table 2. The L_1, L_2, L_3, and $L_{\rm Tot}$ ionization cross sections (kb) for ^{19}F on Os as a function of energy (MeV). TH1, TH2, and TH3 denote the ECUSAR-CSM, the RSCA-CSM, and the SLPA model, respectively, while EC denotes the electron capture.

E	Expt. (σ_{Li})	TH1	TH1 + EC	TH2	TH2 + EC	TH3	TH3 + EC
				$i = 1$			
76	3.3	4.0	4.3	1.9	2.2	2.7	3.0
84	5.6	5.5	5.9	2.7	3.1	3.7	4.1
90	12.0	6.7	7.2	3.4	3.9	4.5	5.0
98	11.3	8.4	9.1	4.3	5.0	5.6	6.3
114	17.6	11.8	12.8	6.3	7.2	8.3	9.3
				$i = 2$			
76	3.0	5.0	5.3	2.4	2.7	3.9	4.2
84	5.2	6.2	6.6	3.1	3.5	4.9	5.3
90	10.6	7.2	7.7	3.6	4.1	5.7	6.2
98	8.4	8.5	9.1	4.4	5.0	6.9	7.5
114	14.3	11.2	12.2	6.0	7.0	9.4	10.4
				$i = 3$			
76	11.4	17.3	17.8	8.3	8.8	14.7	15.2
84	19.0	21.0	21.7	10.3	11.0	17.7	18.4
90	37.5	23.8	24.6	12.0	12.7	20.1	20.9
98	30.0	27.7	28.9	14.2	15.4	23.4	24.6
114	47.0	35.4	37.1	18.8	20.5	30.3	32.0
				$L_{\rm Tot}$			
76	17.7	26.3	27.4	12.7	13.8	21.3	22.4
84	29.8	32.7	34.2	16.1	17.6	26.3	27.8
90	60.1	37.6	39.4	19.0	20.7	30.3	32.1
98	49.6	44.5	47.0	22.9	25.4	35.9	38.4
114	78.9	58.4	61.1	31.0	34.7	48.0	51.7

The inclusion of electron capture has the correct tendency, but it does not account for the discrepancies. It can also be noted from figure 5(A) that the vacancy sharing among the L subshells described by the coupled-states model (CSM) has a minor role in the present collisional system. The uncertainty bound for most accurate theoretical model (ECUSAR-CSM+EC) is shown in figure 5(A), which is estimated using the method discussed in Singh *et al* [54].

The EC cross sections for the L_i subshells as a function of the impact energy are plotted in figure 6. According to the figure, the EC contribution of the L_3 subshell is the largest one, while L_1 and L_2 are of the same order. To estimate these contributions, we used the charge-state distributions of the projectile ions inside the solid target as presented in figure 3.

In a recent article [54], we analyzed the major sources of errors in the measurements of L-subshell cross sections. We concluded that these uncertainties come from four main sources: (i) determination of target

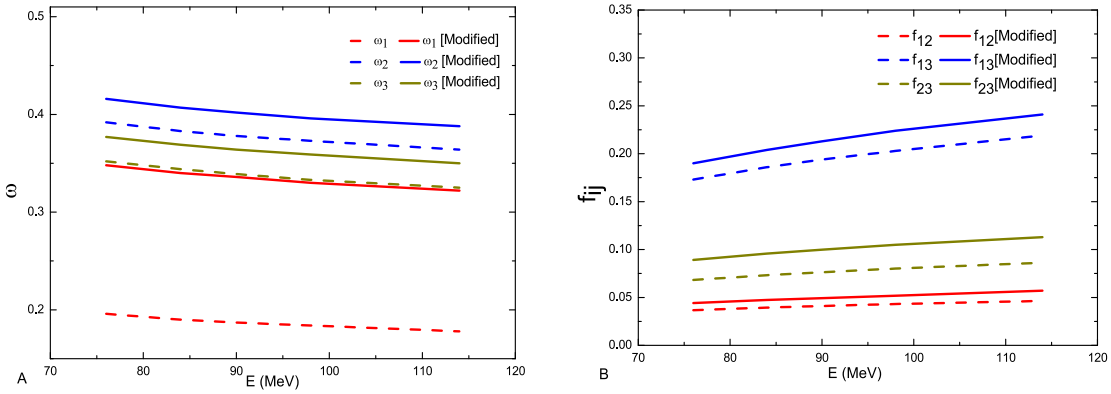

Figure 4. The effect of the simultaneous multiple ionization on the fluorescence yields (A) and Coster-Kronig yields (B). The plotted data are results of calculations using equations (20) to (21), where the atomic parameters for the single ionization condition were taken from [43]. Modified values were optimized in order to have a good agreement between the experimental and theoretical L_i-subshell ionization cross sections.

thickness, (ii) counting the number of projectile particles, (iii) background subtraction during spectrum analysis, and (iv) atomic parameters used for the conversion of x-ray production to L_i-ionization cross sections and vice versa. In this work, all these aspects were considered carefully. The first source of error was managed by measuring the foil thickness by the RBS method, as shown in figure 1. The mass thickness (target thickness in μgcm^{-2}) is normally measured by three techniques viz., RBS, PIXE and XRF (x-ray fluorescence). Out of these, RBS is the most accurate (see figure 4 of Ager *et al* [55]). The second source of uncertainties was controlled by measuring the integrated charge count of the projectile ions in a Faraday cup placed behind the target for a fixed duration (100 s) and under two different conditions: (a) solely the blank target frame in place and (b) the target foil in place. The ratio between the integrated charge counts for the two different conditions is $R = \frac{nq}{nq'} = \frac{q}{q'}$ or $q' = \frac{q}{R}$, where n is the number of projectile ions of incident charge state q in case of blank target, and of charge state q' when the target is in place. If the spectra is recorded for a long duration (say, 30 minutes), then, the total measured charge divided by q' will give the number of projectile ions passing through the target foil as required in equation (1). The third source of error was also considered, as can be evidenced from figures 2: the data points are well on the fitting profile, and the reduced χ-squared values are close to 1.

Finally, about the fourth source of uncertainty, besides the L-shell ionization, heavy ion collisions give rise to simultaneous ionization of the higher-shell electrons. This change of electronic environment in an atom alters the properties of the L x-ray emission. As a result, the atomic parameters vary with the projectile energy as shown in figure 4. Although this effect was taken into account, the L_i subshell-ionization cross sections derived from the measured L x-ray production cross sections are still underestimated by the models, as can be seen in figure 5(A). The atomic parameters are used to convert the L x-ray production cross section to L_i subshell ionization cross section, as discussed above. In general, such parameters are taken from various sources, where the authors have calculated them using different theoretical methods. In some cases, the theoretical predictions considerably deviate from each other. In particular, for ω_1^0, f_{12}^0 and f_{13}^0, a spread of up to a factor of two can be observed, as shown in table 4. The estimated uncertainties for ω_1^0, ω_2^0, ω_3^0, f_{12}^0, f_{13}^0, and f_{23}^0 are 15%, 5%, 5%, 10%, 5%, and 5%, respectively, in the most recent compilation [43]. Hence, such theoretical atomic parameters may pose problem in getting an agreement between the theory and experiment. Accordingly, to resolve the above-mentioned discrepancy between the measurements and the theoretical calculations of the L_i subshell ionization cross sections, we varied these atomic parameters concerning to only a single L-vacancy iteratively until a good agreement was achieved; see figure 4. We present the optimized parameters in table 1 and show their variation with the beam energy in figure 4. The difference between the original [43] values and the optimized values for single vacancy atomic parameters is not significant, except for ω_1^0. This problem with ω_1 can be connected to alteration of the CK transitions (for example L_1-$L_3M_{4,5}$) due to SMI, which can substantially change the x-ray fluorescence.

There are two ways to study the L_i subshell ionization by ion impact: by comparing (i) the theoretical and experimental L_i subshell ionization cross sections, and (ii) the theoretical and experimental L x-ray production cross sections. In the first, the atomic parameters are used to convert the experimental L x-ray production cross sections into L_i subshell ionization cross sections in figure 5(A). Whereas in figure 5(B), the theoretical L_i subshell ionization cross sections are converted to L x-ray production cross sections using the atomic parameters. The theoretical values in figure 5(A) are obtained by employing the set of atomic parameters given in [43]. Here, the uncertainty bound to the best theoretical model (ECUSAR-CSM+EC) has been incorporated

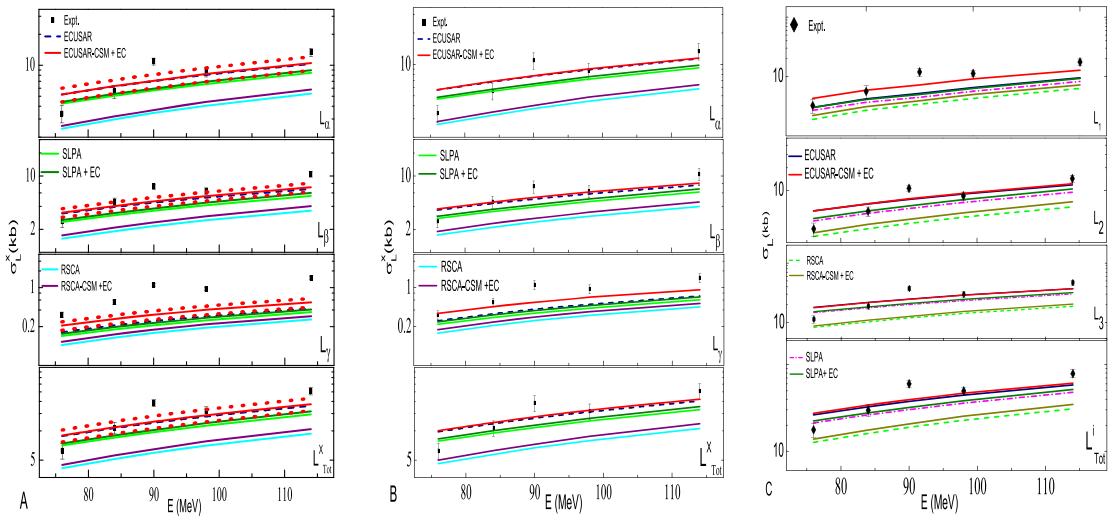

Figure 5. A. Comparison of the measured L_α, L_β, L_γ, and L_{Tot} x-ray production cross sections with the predictions of the different theoretical models. Uncertainty bound for the most accurate theoretical model (ECUSAR-CSM+EC) is denoted by an envelope formed by two dotted red lines. B. Comparison of the measured L_α, L_β, L_γ, and L_{Tot} x-ray production cross sections with the predictions of the different theoretical models by using optimized atomic parameters. C. Experimental and theoretical L_i-subshell ($i = 1 - 3$) and total L-shell ionization cross sections for ^{19}F on Os collisions as a function of the impact energy. The measured data were obtained using optimized atomic parameters.

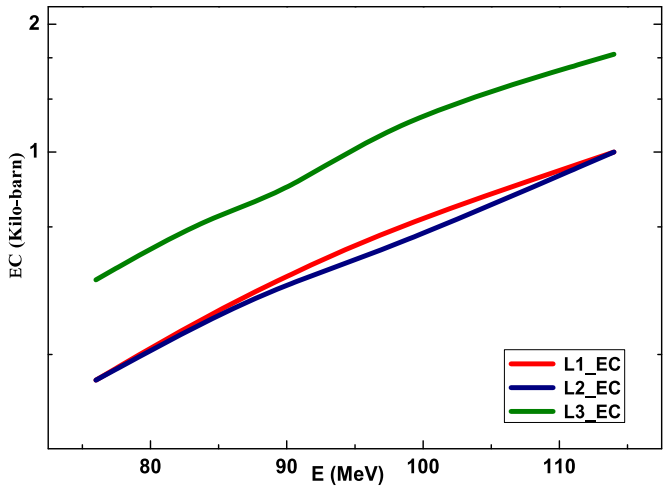

Figure 6. Capture cross sections from the L_i-subshell ($i = 1, 2, 3$) of the Os target to the K shell of the ^{19}F projectile as a function of the impact energy.

here. It shows that the theoretical model is still underestimating the measured L_γ cross sections. Where as the optimized set of atomic parameters gives a good agreement, apart from deviations at 76 and 90 MeV, with all the experimental data as shown in figures 5(B) and 5(C), concerning to the production cross-sections and the ionization cross-sections, respectively.

In fact, deviation larger than the experimental error does not appear only with the 90 MeV data point but also with the 76 MeV data point too. More controlled experiment, as we in a recent work [56], can only shade some light on such issues. Furthermore, any genuine departure leads to significant aspects of physics, for example [57], where besides the usual atomic processes an additional ionization phenomenon induced by nuclear recoils was discovered.

Presumably, the proton beam does not produce SMI in the target and thus the complexity due to the complication of multiple ionization is ruled out. However, in some cases, even the proton induced total L-shell production cross section data do not agree with the theoretical predictions. One of such cases is found in uranium [58], Where the theoretical total L-shell production cross sections differ from the experimental values [59–61] by about a factor of two if the atomic parameters are taken from either Krause [62] or Campbell [44]. If

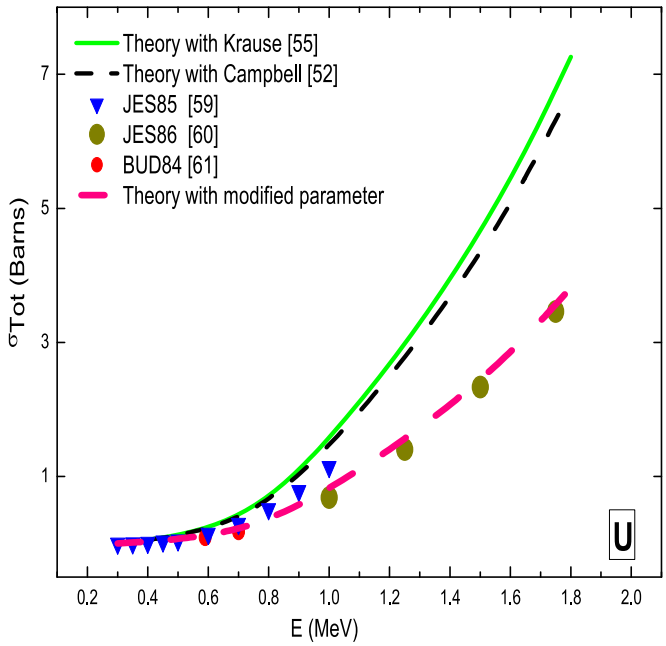

Figure 7. Total L-shell production of uranium by proton impact: the pink dotted line denotes the total L-shell production cross section with optimised atomic parameters $\omega_1 = 48\%$, $\omega_2 = 45\%$, $\omega_3 = 46\%$, $f_{12} = 20\%$, $f_{13} = 10\%$, $f_{23} = 15\%$ of the corresponding parameter of Campbell [44].

Table 3. The L_α, L_β, L_γ, and L_{Tot} x-ray production cross sections for ^{19}F on Os as a function of energy. Same notation and units as table 2.

E	Expt. (σ_L^x)	TH1	TH1 + EC	TH2	TH2 + EC	TH3	TH3 + EC
				Ll			
76	0.27	0.27	0.28	0.13	0.14	0.22	0.23
84	0.37	0.32	0.33	0.16	0.17	0.27	0.28
90	0.44	0.36	0.37	0.18	0.19	0.30	0.31
98	0.45	0.42	0.44	0.21	0.23	0.35	0.37
114	0.63	0.53	0.56	0.28	0.31	0.45	0.47
				L_α			
76	3.4	5.04	5.2	2.42	2.58	4.24	4.40
84	5.56	6.05	6.27	2.97	3.19	5.05	5.27
90	10.90	6.80	7.07	3.44	3.66	5.69	5.94
98	8.65	7.91	8.25	4.04	4.41	6.58	6.94
114	13.40	9.97	10.50	5.30	5.81	8.43	8.95
				L_β			
76	2.55	3.16	3.33	1.51	1.67	2.50	2.65
84	4.61	3.85	4.04	1.89	2.11	3.06	3.26
90	7.28	4.42	4.65	2.20	2.46	3.50	3.75
98	6.33	5.16	5.45	2.63	2.97	4.13	4.46
114	10.6	6.67	7.12	3.52	4.04	5.49	5.99
				L_γ			
76	0.33	0.19	0.34	0.15	0.18	0.22	0.24
84	0.55	0.26	0.46	0.21	0.24	0.30	0.32
90	1.13	0.30	0.55	0.26	0.30	0.35	0.39
98	0.95	0.37	0.67	0.32	0.37	0.43	0.48
114	1.51	0.50	0.92	0.45	0.52	0.61	0.68
				L_{Tot}			
76	6.28	10.02	10.20	4.62	5.00	7.90	8.26
84	10.70	12.15	12.20	5.74	6.28	9.49	10.01
90	19.30	12.87	13.90	6.69	7.28	10.79	11.40
98	15.90	14.85	16.32	7.92	8.79	12.61	13.44
114	25.50	18.77	21.04	10.53	11.78	16.45	17.70

Table 4. Fluorescence and CK yields for singly ionized element from different theories.

$_{76}$Os	Fluorescence Yield			CK Yield		
	ω_1^0	ω_2^0	ω_3^0	f_{12}^0	f_{13}^0	f_{23}^0
Krause [62]	0.130	0.295	0.281	0.16	0.39	0.128
Chen *et al* [63]	0.088	0.318	0.282	0.088	0.636	0.136
Orlić *et al* [64]	0.13	0.295	0.281	0.16	0.39	0.128
Campbell [43]	0.15	0.318	0.282	0.07	0.33	0.13

we use the optimized set of atomic parameters, the agreement between the experiment and theory becomes excellent. Hence, the optimization of atomic parameters is validated by the proton induced total L-shell production cross section data of uranium [58], as shown in figure 7.

Furthermore, from the values in tables 2 and 3, we notice that the agreement between the theory and experiment is better for the L_i subshell ionization cross sections rather than the L x-ray production cross sections. Thus, the differential comparison provides a better picture than the integral one.

7. Conclusions

In the present work, the L x-ray production cross sections of Os were measured by five different beam energies of $^{19}F^q$ ions with charge states $q = 6+, 7+$ and $8+$ in the energy range of 4–6 MeV/u. Different ionization theories such as RSCA, ECUSAR and SLPA were implemented to compute the direct ionization. Additionally, the contribution of the LK electron capture was added to each theory. The effect of multiple ionization was also considered by modifying the atomic parameters. Furthermore, L_i $(i = 1, 2, 3)$ subshell ionization cross sections were derived from the measured L x-ray production cross sections, and compared with the corresponding theoretical counterparts. Electron capture (EC) and coupled states among L-subshells (CSM) proved to have a minor role in the present results. Both comparisons show the best agreement for the ECUSAR model with the experimental data followed by the abinitio SLPA. However, certain differences are still clearly noticed. Change of atomic parameters due to SMI is incorporated. However, this is not sufficient to obtain a good agreement between the theory and experiment. These results cast doubts on the theoretically obtained original atomic parameters due to single vacancy only. To resolve such discrepancies, the atomic parameters were optimized to obtain a good agreement between the measurement and ECUSAR-CSM-EC model. Thus, this work gives us a convincing understanding of the L-subshell ionization mechanism by heavy ion bombardments if the atomic parameters used in the conversion of the x-ray production cross sections to the ionization cross sections are put under scrutiny. Hence, our work suggests the urgent need for accurate measurements and theoretical calculations of the atomic parameters. Now the question is whether the parameters commonly used until now are correct. This aspect can be examined by reexamining the data. The heavy ion induced data can be treated in the way as done here. The photon or proton induced data, where the simultaneous multiple ionization effect is almost null and ECPSSR theory is expected to describe the L-subshell ionization phenomenon satisfactorily. Hence, any disparity between the theory and experiment can be ascribed to incorrect atomic parameters and the parameters for those cases can be optimized with the current approach. Such optimized parameters need to be checked by an improved theory and developing such a theory is a current challenge for theoreticians.

Acknowledgments

The authors are grateful to the Pelletron staff for the smooth conduct of the experiments and the RBS lab for the target thickness measurements. S.C. acknowledges the University of Kalyani for providing generous funding towards his fellowship. Financial support from the Science and Engineering Research Board (SERB), New Delhi (SB/FTP/PS-023/2014), to Sunil Kumar in terms of Young Scientist scheme, and the grant from IUAC, New Delhi (UF-UP-43302 project), are highly acknowledged. L. Sarkadi acknowledges the support from the Hungarian Scientific Research Fund (Grant No. K128621). A.M.P. Mendez, D.M. Mitnik and C.C. Montanari acknowledge the financial support from the following institutions of Argentina: Consejo Nacional de Investigaciones Científicas y Técnicas (CONICET), Agencia Nacional de Promoción Científica y Tecnológica (ANPCyT), and Universidad de Buenos Aires (UBA).

ORCID iDs

A M P Mendez https://orcid.org/0000-0003-3568-7730
D M Mitnik https://orcid.org/0000-0003-0193-0958
C C Montanari https://orcid.org/0000-0002-7325-6125
L Sarkadi https://orcid.org/0000-0002-5763-2063
T Nandi https://orcid.org/0000-0001-8577-9102

References

[1] Satoh T 2015 Development of particle induced x-ray emission-computed tomography in takasaki advanced radiation research institute, japan atomic energy agency *Int. J. PIXE* **25** 147–52
[2] Sharma P and Nandi T 2016 Experimental evidence of beam-foil plasma creation during ion-solid interaction *Phys. Plasmas* **23** 083102
[3] Dyson N A and Dyson N A 1990 *X-rays in Atomic and Nuclear Physics* (Cambridge: Cambridge University Press)
[4] Antoszewska-Moneta M, Brzozowski R and Moneta M 2015 Modification of thin films induced by slow heavy ions analysed with PIXE and SRIM *Eur. Phys. J.* D **69** 1–6
[5] Gillespie A W, Phillips C L, Dynes J J, Chevrier D, Regier T Z and Peak D 2015 Advances in using soft X-Ray spectroscopy for measurement of soil biogeochemical process *Advances in Agronomy* **133** 1–32
[6] Johansson T B, Akselsson R and Johansson S A 1970 x-ray analysis: Elemental trace analysis at the 10^{-12} g level *Nucl. Instrum. Methods* **84** 141–3
[7] Bertol A, Hinrichs R and Vasconcellos M 2015 Proton induced L1, L2, L3-sub-shell x-ray production cross sections of Hf and Au *Nucl. Instrum. Methods Phys. Res., Sect. B* **363** 28–32
[8] Garcia J 1970 Inner-shell ionizations by proton impact *Phys. Rev.* A **1** 280
[9] Joseph D, Rao S N and Kailas S 2013 Measurement of L X-Ray production cross-sections of Au, Ho, Bi and K-X-Ray cross sections of Nb, Sn, Sb by using protons of energy 4 Mev *Mapana Journal of Sciences* **12** 1–8
[10] Zhou X, Zhao Y, Cheng R, Wang Y, Lei Y, Wang X and Sun Y 2013 K and L-shell x-ray production cross sections for 50–250 keV proton impact on elements with Z = 26–30 *Nucl. Instrum. Methods Phys. Res., Sect. B* **299** 61–7
[11] Miranda J, Murillo G, Méndez B, López-Monroy J, Aspiazu J, Villaseñor P, Pineda J and Reyes-Herrera J 2013 Measurement of L x-ray production cross sections by impact of proton beams on Hf, Ir, and Tl *Nucl. Instrum. Methods Phys. Res., Sect. B* **316** 113–22
[12] Miranda J and Lapicki G 2014 Experimental cross sections for L-shell x-ray production and ionization by protons *At. Data Nucl. Data Tables* **100** 651–780
[13] Mohan H, Jain A K, Kaur M, Singh P S and Sharma S 2014 Cross section for induced L x-ray emission by protons of energy <400 keV *Nucl. Instrum. Methods Phys. Res., Sect. B* **332** 103–5
[14] Siegele R, Cohen D D and Dytlewski N 1999 The ANSTO high energy heavy ion microprobe *Nucl. Instrum. Methods Phys. Res., Sect. B* **158** 31–8
[15] Raju G N, Murty G R, Reddy B S, Reddy T S, Lakshminarayana S and Reddy S B 2004 Multiple ionization effects on L x-ray intensity ratios in Hf, Ta, Re, Ir, Pt, Au and Pb due to proton bombardment at energies 1-5 Mev *The European Physical Journal D-Atomic, Molecular, Optical and Plasma Physics* **30** 171–9
[16] Uchai W, Lapicki G, Milner W, Raman S, Rao P V and Vane C 1985 L x-ray emission from high-z elements after ionisation by 1 MeV u-1 ag ions *J. Phys. B: At. Mol. Phys.* **18** L389
[17] Murillo G, Méndez B, López-Monroy J, Miranda J and Villaseñor P 2016 L-shell x-ray production cross sections of Ce, Nd, Sm, Eu, Gd, and Dy by impact of $^{14}N^{2+}$ ions with energies between 7.0 Mev and 10.5 Mev *Nucl. Instrum. Methods Phys. Res., Sect. B* **383** 89–92
[18] Fijał-Kirejczyk I *et al* 2008 Coupling and binding-saturation effects in L-subshell ionization of heavy atoms by 0.3-1.3-Mev/amu Si ions *Phys. Rev.* A **77** 032706
[19] Pajek M *et al* 2015 L x-ray emission induced by heavy ions *Nucl. Instrum. Methods Phys. Res., Sect. B* **363** 19–23
[20] Chatterjee S, Sharma P, Singh S, Oswal M, Kumar S, Montanari C, Mitra D and Nandi T 2021 Significance of the high charge state of projectile ions inside the target and its role in electron capture leading to target-ionization phenomena *Phys. Rev.* A **104** 022810
[21] Mendez A M P, Montanari C C and Mitnik D M 2019 Relativistic atomic structure calculations of heavy targets for inelastic collisions *Nucl. Instrum. Methods Phys. Res., Sect. B* **460** 114–8
[22] Kumar S, Singh U, Oswal M, Singh G, Singh N, Mehta D, Nandi T and Lapicki G 2017 L shell x ray production in high-Z elements using 4–6 MeV/u fluorine ions *Nucl. Instrum. Methods Phys. Res., Sect. B* **395** 39–51
[23] Oswal M *et al* 2020 Experimental and theoretical l-shell ionization cross sections of heavy atoms by impact of si ions *Radiat. Phys. Chem.* **176** 108809
[24] Berger M 1998 *Xcom: Photon Cross Sections Database (nbsir 87-3597)* (National Institute of Standards and Technology) (http://physics.nist.gov/PhysRefData/Xcom/Text/Xcom.html)
[25] Ziegler J F, Ziegler M D and Biersack J P 2010 SRIM-the stopping and range of ions in matter (2010) *Nucl. Instrum. Methods Phys. Res., Sect. B* **268** 1818–23
[26] Subramaniam E and Kumar B 2010 Data Acquisition Systems-Current and future trends dae symp *J Nucl. Phys.* **69** 117–20
[27] Marquardt D W 1963 An algorithm for least-squares estimation of nonlinear parameters *Journal of the Society for Industrial and Applied Mathematics* **11** 431–41
[28] Sarkadi L and Mukoyama T 1984 Higher order processes in L-shell ionization *Nucl. Instrum. Methods Phys. Res., Sect. B* **4** 296–302
[29] Lugosi L and Sarkadi L 2001 Calculation of the matrix elements of the Coulomb interaction involving relativistic hydrogenic wave functions *Comput. Phys. Commun.* **141** 73–82
[30] Brandt W and Lapicki G 1981 Energy-loss effect in inner-shell coulomb ionization by heavy charged particles *Phys. Rev.* A **23** 1717
[31] Lapicki G 2002 The status of theoretical L-subshell ionization cross sections for protons *Nucl. Instrum. Methods Phys. Res., Sect. B* **189** 8–20
[32] Montanari C, Mitnik D and Miraglia J 2011 A collective model for inner shell ionization of very heavy targets *Radiat. Eff. & Defects in Solids* **166** 338–45
[33] Montanari C and Miraglia J 2013 Theory of heavy ion collision physics in hadron therapy *Adv. Quantum Chem.* **65** 165–201
[34] Sarkadi L and Mukoyama T 1988 Subshell coupling effects in L-shell ionization of gold by proton impact *Phys. Rev.* A **37** 4540

[35] Sarkadi L and Mukoyama T 1990 Dynamical subshell coupling effects in L-shell ionization of thorium by heavy ions *J. Phys. B: At. Mol. Opt. Phys.* **23** 3849
[36] Lapicki G, Murty G R, Raju G N, Reddy B S, Reddy S B and Vijayan V 2004 Effects of multiple ionization and intrashell coupling in L-subshell ionization by heavy ions *Phys. Rev.* A **70** 062718
[37] Levine Z H and Louie S G 1982 New model dielectric function and exchange-correlation potential for semiconductors and insulators *Phys. Rev.* B **25** 6310
[38] Klapisch M 1967 *Acad. Sci.* **265** 914
[39] Klapisch M 1971 A program for atomic wavefunction computations by the parametric potential method *Comput. Phys. Commun.* **2** 239–60
[40] Bar-Shalom A, Klapisch M and Oreg J 2001 Hullac, an integrated computer package for atomic processes in plasmas *J. Quant. Spectrosc. Radiat. Transfer* **71** 169–88 radiative Properties of Hot Dense Matter
[41] Oswal M, Kumar S, Singh U, Singh G, Singh K, Mehta D, Mitnik D, Montanari C C and Nandi T 2018 L x-ray production cross sections in high-Z atoms by 3–5 MeV/u silicon ions *Nucl. Instrum. Methods Phys. Res., Sect. B* **416** 110–8
[42] Campbell J and Wang J-X 1989 Interpolated dirac-fock values of l-subshell x-ray emission rates including overlap and exchange effects *At. Data Nucl. Data Tables* **43** 281–91
[43] Campbell J 2003 Fluorescence yields and Coster-Kronig probabilities for the atomic L subshells *At. Data Nucl. Data Tables* **85** 291–315
[44] Campbell J 2009 Fluorescence yields and Coster-Kronig probabilities for the atomic L subshells. part ii: the L1 subshell revisited *At. Data Nucl. Data Tables* **95** 115–24
[45] Lapicki G, Mehta R, Duggan J L, Kocur P, Price J and McDaniel F D 1986 Multiple outer-shell ionization effect in inner-shell x-ray production by light ions *Phys. Rev.* A **34** 3813
[46] Pajek M *et al* 2003 Multiple ionization and coupling effects in L-subshell ionization of heavy atoms by oxygen ions *Phys. Rev.* A **68** 022705
[47] Lapicki G and Losonsky W 1977 Electron capture from inner shells by fully stripped ions *Phys. Rev.* A **15** 896
[48] May R 1964 An algorithm for least-squares estimation of nonlinear parameters *Appl Math* **11** 431–41
[49] Brandt W, Laubert R, Mourino M and Schwarzschild A 1973 Dynamic Screening of Projectile Charges in Solids Measured by Target X-Ray Emission *Phys. Rev. Lett.* **30** 358
[50] Schiwietz G and Grande P 2001 Improved charge-state formulas *Nucl. Instrum. Methods Phys. Res., Sect. B* **175** 125–31
[51] Sharma P and Nandi T 2019 Disentangling the bulk and exit surface contribution on projectile-charge-state evolution *Physical Review Accelerators and Beams* **22** 034501
[52] Nandi T 2008 Formation of the circular rydberg states in ion-solid collisions *Astrophys. J. Lett.* **673** L103
[53] Novikov N and Teplova Y A 2014 Methods of estimation of equilibrium charge distribution of ions in solid and gaseous media *Phys. Lett.* A **378** 1286–9
[54] Singh S, Chatterjee S, Mitra D and Nandi T 2021 Evaluation of accurate uncertainty of measurement in L subshell ionization cross-section arXiv:2103.07247
[55] Ager F, Ferretti M, Grilli M, Juanes D, Ortega-Feliu I, Respaldiza M, Roldán C and Scrivano S 2017 Reconsidering the accuracy of x-ray fluorescence and ion beam based methods when used to measure the thickness of ancient gildings *Spectrochim. Acta, Part B* **135** 42–7
[56] Singh S, Chatterjee S, Mitra D and Nandi T 2022 Evaluation of accurate uncertainty of measurement of l subshell ionization cross-sections *Measurement* **187** 110322
[57] Sharma P and Nandi T 2017 Shakeoff ionization near the coulomb barrier energy *Phys. Rev. Lett.* **119** 203401
[58] Orlic I, Sow C and Tang S 1994 Experimental l-shell x-ray production and ionization cross sections for proton impact *At. Data Nucl. Data Tables* **56** 159–210
[59] Jesus A, Lopes J and Ribeiro J 1985 L-shell x-ray production cross sections for au, pb and u by proton, deuteron and alpha impact *J. Phys. B: At. Mol. Phys.* **18** 2453
[60] Jesus A, Pinheiro T, Niza I, Ribeiro J and Lopes J 1986 L-shell x-ray production cross sections for pixe analysis of elements from ag to u *Nucl. Instrum. Methods Phys. Res., Sect. B* **15** 595–7
[61] Budnar M, Cindro V, Kregar M, Ravnikar M, Ramšak V and Šmit Z Š 1984 Measurements of proton induced l shell x-ray cross sections on thin lu, w, au, tl, pb, th and u targets *Nucl. Instrum. Methods Phys. Res., Sect. B* **3** 39–42
[62] Krause M O 1979 Atomic radiative and radiationless yields for k and l shells *J. Phys. Chem. Ref. Data* **8** 307–27
[63] Chen M H, Crasemann B and Mark H 1981 Widths and fluorescence yields of atomic L-shell vacancy states *Phys. Rev.* A **24** 177
[64] Orlić I, Sow C and Tang S 1994 Semiempirical formulas for calculation of L subshell ionization cross sections *Int. J. PIXE* **4** 217–30